

LumiPath – Towards Real-time Physically-based Rendering on Embedded Devices

Laure Fink^{1,2}, Sing Chun Lee¹, Marc Stamminger², Nassir Navab¹, and Mathias Unberath¹

¹ Johns Hopkins University

² Friedrich-Alexander University Erlangen-Nuremberg

Send communication to unberath@jhu.edu.

Abstract. As the computational power of today’s devices increases, real-time physically-based rendering becomes possible, and is rapidly gaining attention across a variety of domains. These include gaming, where physically-based rendering enhances immersion and overall entertainment experience, all the way to medicine, where it constitutes a powerful tool for intuitive volumetric data visualization. However, leveraging the obvious benefits of physically-based rendering (also referred to as photo-realistic rendering) remains challenging on embedded devices such as optical see-through head-mounted displays because of their limited computational power, and restricted memory usage and power consumption. We propose methods that aim at overcoming these limitations, fueling the implementation of real-time physically-based rendering on embedded devices. We navigate the compromise between memory requirement, computational power, and image quality to achieve reasonable rendering results by introducing a flexible representation of plenoptic functions and adapting a fast approximation algorithm for image generation from our plenoptic functions. We conclude by discussing potential applications and limitations of the proposed method.

Disclaimer: This manuscript describes work in progress.

Keywords: Physically-based Rendering · Light Field · Fibonacci · Embedded · Plenoptic Function · Augmented Reality · Mixed Reality

1 Introduction

1.1 Real-time Physically-based Rendering

Conventional rasterization methods generate images by shading objects artificially and mostly limit considerations to direct illumination. This is in contrast to physically-based rendering that aims at synthesizing images by accurately mimicking light propagation. To this end, these methods consider how light quanta are emitted from light sources, bounce around a 3D scene governed by physical laws, and eventually impinge on the camera’s image plane forming a realistic image. As a direct consequence, physically-based rendering additionally provides

indirect illumination effects which have a high impact on perceived realism, motivating its more colloquial name: Photo-realistic rendering. One such method, *ray tracing* [17], simulates light rays in a reverse order, solving the well known rendering equation [10]:

$$L_o(x, \omega_o, \lambda, t) = L_e(x, \omega_o, \lambda, t) + \int_{\Omega} f_r(x, \omega_i, \lambda, t) L_i(x, \omega_i, \lambda, t) \cos \theta_i \, d\omega_i. \quad (1)$$

Incoming radiance is integrated for each pixel by following rays that are emitted from the camera center. These rays hit surfaces and media in the scene which they interact with based on the physical simulation of illumination such as reflection, refraction, and shadowing. From these hit-points, again all incoming radiance is integrated and rays are repeatedly traced until they eventually reach a light source (or exit the scene).

Accurately accounting for imaging physics can result in images that are indistinguishable from the real world and provide quality that is barely achievable by purely rasterized images. From the above description of physically-based rendering it should have become apparent that these approaches to rendering are computationally very expensive. This shortcoming limits their presence in consumer-grade applications since real-time image generation, as it is required for most applications, was near impossible. Current hardware, like the *Nvidia GeForce RTX*, made a big step towards real-time ray tracing by incorporating deep learning technology into the rendering process, drastically reducing the required computations. This is achieved by aggressively limiting light-scene interactions and restricting the horizon, the resulting artifacts of which can be masked with machine learning-based post-processing.

The aforementioned increase in compute capabilities of *graphics processing units* (GPUs) and advances of rendering algorithms have fueled the recent interest in adopting real-time physically-based rendering in daily applications such as gaming, movie making, and medical visualization. Unfortunately, these advances do not translate well to applications that run on embedded devices, such as optical see-through head-mounted displays, tablets, or smartphones. This is because 1) state-of-the-art GPU hardware cannot easily be miniaturized and integrated, and 2) remote-computation and streaming is not necessarily a desirable option (particularly in the medical context). In the remainder of this manuscript, we present descriptions of *work-in-progress* methods that aim at bringing real-time physically-based rendering to embedded devices.

1.2 Related Work

Plenoptic Function Representations Without a powerful GPU, like the *Nvidia GeForce RTX*, on portable devices for sophisticated rendering algorithms, we consider an alternative approach – reconstructing plenoptic functions.

Gathering radiance information in a 3D static scene can be expressed as tracing the set of all possible rays, defined by their origin $(x, y, z) \in \mathbb{R}^3$ and arbitrary direction $(\theta, \phi) \in [0, \pi] \times [0, 2\pi]$, yielding five degrees of freedom (DoFs). This

way of describing the flow of light is referred to as *light field* [6] or *plenoptic function* [2,14]. Interestingly, the exact same concerns raised above, namely hardware limitations, led to considerations of precomputing a subset of the plenoptic function in a domain of interest rather than solving the complex rendering equation on the fly. Image synthetization is then performed by sampling and interpolating the radiance information from the precomputed results which is then referred to as *image based rendering* in literature [13].

Among the most well-known representatives of such approaches is the so-called LumiGraph [8], which reduces the five DoFs of the plenoptic function to four. The Lumigraph is based on the assumption that medium surrounding medium an object of interest is completely transparent (radiance is constant along the ray), and that therefore, the plenoptic function can be parameterized in terms of a bounding surface, namely a cube. By heavily constraining possible camera-object arrangements, this surface can be further reduced by only considering two opposite sides of the cube, i. e. two planes. A point set P_o discretizes the first plane. A second point set P_d discretizes the second plane. The set of precomputed rays can then be determined by connecting every point $p_o \in P_o$ with each point $p_d \in P_d$. This arrangement may lead to artifacts [3] because of biased sampling ray directions.

Several others followed Gortler et al.’s considerations and investigated different geometrical primitives for parameterization. Camahort et al. [3] examined a sphere as primitive to provide more uniformly sampled light fields. They perform a binning approach based on a Bresenham-style discretization of the spherical surface which introduces two drawbacks: First, this sampling scheme is not perfectly uniform, and second, retrieving radiance information back from the data structure has linear time complexity and is dependent on the number of bins. This suggests that rendering time substantially increases with higher resolution, since both the number of rays as well as the retrieval time per ray increases.

Physically-based Rendering on Embedded Devices The only other work (in form of a patent [22] and a press release [1]) that aims at achieving physically-based rendering on embedded devices, such as head-mounted displays, is out of Siemens Healthineers, who have been pushing the implementation of photo-realistic rendering in volumetric medical image visualization [4]. Since current information on the proposed technology is limited, *we hypothesize* that this method is similar to plenoptic functions in that it front-loads computations to accelerate image generation, but quite different otherwise. Front-loading is achieved by first, generating *many* images at various camera poses from a 3D scene (in this case, a voxelized 3D volume such as a CT scan) using a state-of-the-art physically-based rendering pipeline. These images then serve as input to an iterative ”reconstruction” algorithm similar to the ones used in conventional CT reconstruction [7] from X-ray projection images. In this process, the CT intensity values are iteratively updated such that simple ray casting schemes through the volume, which are fast but not physically-based, will reproduce the physically-based target image. During the application and as the user moves around the object to be rendered, simple ray casting will generate images that mimic the photo-realistic

effect. A positive aspect of this approach would be that the process of altering CT intensity values can be expressed as a non-linear, shift-variant 3D filtering operation. This means that such operation could, in principle, be performed by applying a convolutional neural network making the front-loaded computation very fast. Conversely, image generation during application phase still relies on real-time ray casting, which first, we have found to be a quite demanding task for today’s head-mounted displays in its own right [9], and second, does not seem to provide true physically-based rendered images.

1.3 Contributions

In summary, our distinguishable contributions are:

- An algorithm that allows for real-time physically-based rendering-like results on embedded devices, which, to the best of our knowledge, is the first algorithm to do so.
- A new 2D plenoptic function representation using two *Spherical Fibonacci point sets* [12], which are sampled uniformly and with arbitrary sampling size providing flexibility in tweaking memory to any embedded device.
- Using an extended version of the *Inverse Fibonacci Mapping* [11] for fast neighborhood query on our sampling domain. Our query is constant in time and does not require additional query structures. This implies that our rendering algorithm’s run-time complexity is independent of the sampling size, and only depends on the output image size.

2 Method

As mentioned previously, the computational power on embedded devices is often limited for the sake of energy efficiency. Further, the accessible memory of a single application is restricted for resource balancing among all applications running on the device. In order to allow for physically-based rendering on such devices, we follow the literature and introduce a two-step algorithm, where we first reduce the plenoptic function to a new representation and save its values as a texture, which trades-off hardware resources for rendering quality. And second, using this new representation, we transform the computationally expensive rendering task into a data query and interpolation task, that is fast and provides adequate rendering results.

2.1 Parameterization and Discretization of the Plenoptic Function

The assumptions of the plenoptic function $L(x, y, z, \theta, \phi)$ of a static scene and its representations are depicted in Fig. 2. Our underlying idea is to sample a reparameterized plenoptic function at discretized coordinates in a domain of interest and save the outcome in a 2D texture. An elaborate description of this process, as shown in Fig. 2, is provided in the remainder of this section.

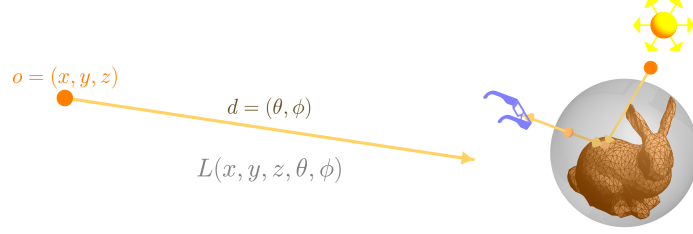


Fig. 1. Assumptions of a LumiGraph. Left: $L(x, y, z, \theta, \phi)$ quantized as a ray with origin $o = (x, y, z)$ and direction $d = (\theta, \phi)$. Right: In transparent media, radiance along a ray remains constant. Thus, the radiance at the intersection point of a ray with a bounding sphere is equal to the radiance that was originally reflected from a point at a surface.

For notation, we use the common conversion C in order to transfer a unit vector v from polar to Cartesian coordinates:

$$v = (x, y, z)^T = C(\theta, \phi) = (\cos(\phi) \sin(\theta), \sin(\phi) \sin(\theta), \cos(\theta))^T. \quad (2)$$

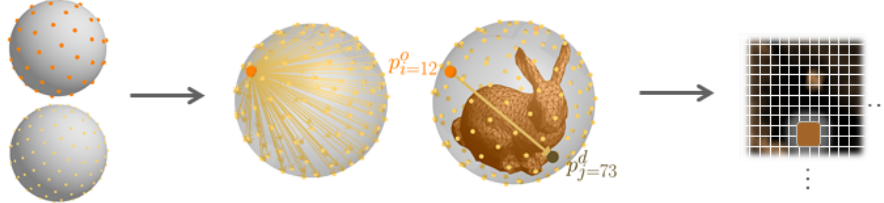


Fig. 2. $\hat{L}(i, j)$ and filling the texture. The surface of the bounding sphere \mathbf{S} is discretized by the two point sets P_o^M and P_d^N . Rays are traced from each p_i^o to each p_j^d resulting in a re-parameterization and discretization of the plenoptic function, referred to as $\hat{L}(i, j)$. The value of $\hat{L}(i, j)$ is written to a 2D texture at position (i, j) .

We use a sphere as geometric primitive to parameterize the plenoptic function L , which reduces its domain to the surface of a bounding sphere \mathbf{S} with a radius R and an origin O around an object of interest. For uniform discretization of the spherical surface \mathbf{S} , *Spherical Fibonacci point sets* P_{SF}^n [12] are chosen. A point p_i of a Spherical Fibonacci point set P_{SF}^n is given by

$$p_i = C(\phi_i, \cos^{-1}(z_i)), \quad (3)$$

$$\phi_i = 2\pi \left\lceil \frac{i}{\Phi} \right\rceil, z_i = 1 - \frac{2i+1}{n}, i \in \{0, \dots, n-1\}, \quad (4)$$

where $[x]$ is the fractional part of x : $[x] = x - \lfloor x \rfloor$. To allow for a distinct amount of possible ray origins and directions, we have two *Spherical Fibonacci point sets* P_o^M and P_d^N , where N is the number of ray origins o , whereas M is the number of directions d .

In our case, the set of all rays traced R^K , is determined by the two spherical Fibonacci point sets P_o^M and P_d^N . The each-to-each connection of P_o^M and P_d^N yields $N \times M$ as the cardinality of R^K . To make things explicit in respect to the parameters of the sphere \mathbf{S} , a ray $r_k \in R^K$ can be calculated by

$$r_k = (O + Rp_i^o) + t\hat{d}_{i,j}, \text{ where } d_{i,j} = p_j^d - p_i^o, \quad (5)$$

$i \in \{0, \dots, N - 1\}$ and $j \in \{0, \dots, M - 1\}$.

The rays in R^K act as camera rays for the path tracing algorithm. The resulting camera can be compared to a reversed version of artificial cameras, which are used to generate spherical environment maps. Following this ray setup, the actual path tracing algorithm is straight forward. The path tracer is comparable to Pharr et al.'s [16] and uses next event estimation.

The captured radiance information for a ray is stored in a two dimensional texture. Each dimension of the texture corresponds to one of the point sets P_o^M and P_d^N and thus, the indices i and j not only identify a point given by the Fibonacci sequence but also the texel coordinates for memory accesses. Therefore, our reparameterized, discrete form of the plenoptic function is in fact 2D (parameterized by 2 indices of the point sets), denoted by $\hat{L}(i, j)$.

2.2 Efficient Image Generation from Our Plenoptic Function

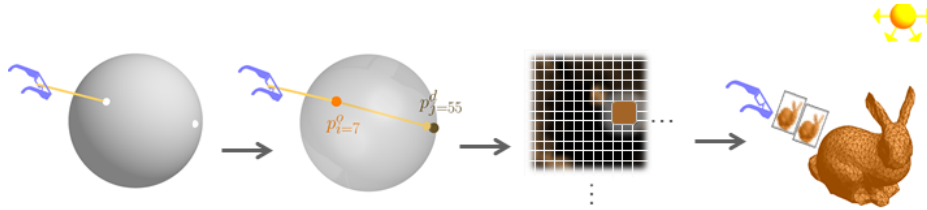


Fig. 3. Process of image synthetization by sampling $\hat{L}(i, j)$. A rasterization ray yields two hitpoints h_o and h_d (white dots). In case of nearest sampling, h_o and h_d are mapped to their nearest neighbors p_i^o and p_j^d . (i, j) in the point sets P_o^M and h_d from P_d^N are used as coordinates to fetch a texel from the texture, and thus sampling $\hat{L}(i, j)$. The mapping is performed for each pixel of the displayed image.

To synthesize images, we want to retrieve the precomputed physically-based rendering result from $\hat{L}(i, j)$ during the rasterization process which is performed on the embedded device. Fig. 3 provides an overview of this process.

The whole image generation process is described in detail as follows:

For each rasterization ray that hits the sphere \mathbf{S} , we find two hit points, namely h_o , for the front face, and h_d , for the back face (hits of tangential rays are discarded). Given a point h on the sphere \mathbf{S} , we can make use of the inverse mapping proposed by Keinert et al. [11] to find the nearest neighbor in a given Spherical Fibonacci point set \mathbf{P} at constant time. Hence, a simple nearest neighbor sampling of \hat{L} is performed by querying the indices of the nearest neighbors of h_o from \mathbf{P}_o^M and h_d from \mathbf{P}_d^N , denoted by i and j , and retrieving the sampled value $\hat{L}(i, i)$ from our plenoptic function.

However, nearest neighbor sampling is piece-wise constant and, thus results in a rather unpleasant appearance. By altering the inverse mapping by Keinert et al. [11], up to nine neighbors of a point h can be queried instead of only the nearest one. At the cost of additional memory accesses, this allows for taking into account multiple samples of \hat{L} . We chose to use up to five neighbors for each point h_o and h_d which results in up to 25 samples of \hat{L} per pixel of the resulting image. Samples are weighted according to the distance of the original hitpoints to their queried neighbors via a filter kernel of size $\sqrt[4]{5} \sqrt{\frac{4\pi}{\sqrt{5}N}}$, where N is the size of the Spherical Fibonacci point set. As the inverse mapping has constant time complexity and the number of samples is fixed, our image generation algorithm has constant time complexity for each pixel. Representative images obtained with this method are presented in Fig. 4.

3 Results

In Fig. 4 we show representative images that were synthesized using a conventional path tracer and our *LumiPath* plenoptic function, respectively. The cardinality of the point sets \mathbf{P}_o^M and \mathbf{P}_d^N were set to $M = 12288$ and $N = 24576$, with points of \mathbf{P}_o^M limited to the upper hemisphere. Consequently, the precomputed texture had a size of 576 MB ($0.5 \times 12288 \times 24576 \times 4$ Byte). We evaluated our rendering results with respect to the conventionally path traced image using quantitative image quality metrics, namely the *Structural Similarity Index* (SSIM) [21] and the *Complex Wavelet SSIM* [19], which are commonly used for image quality assessment [20]. Local SSIM errors are depicted in Fig. 4. In contrast to the SSIM, the CWSSIM performs a complex wavelet transform of the image to a steerable pyramid (with 8 levels in total [19]) prior to the analysis of contrast, structure and luminance. Therefore, the CWSSIM is especially interesting for our use case as utilizing the *LumiPath* alters color results mainly in higher frequency domains, e. g. along edges and specular highlights. This behavior is visualized Fig. 4. The mean quality assessment results for five view angles (see Fig. 4) from different distances (2 and 3 units) was 0.9415 SSIM and 0.9746 CWSSIM (both using the recommended parameter settings [21,19]).

Our path tracing framework producing the ground truth as well as *LumiPath* texture is based on the NVidia Optix Engine [15].

Finally, We evaluated the performance of a first naïve prototype on the Microsoft HoloLens v1. In the worst case scenario, i. e. when the sphere covers all pixels of the displayed image, we achieved a framerate of 2×10 fps for views with

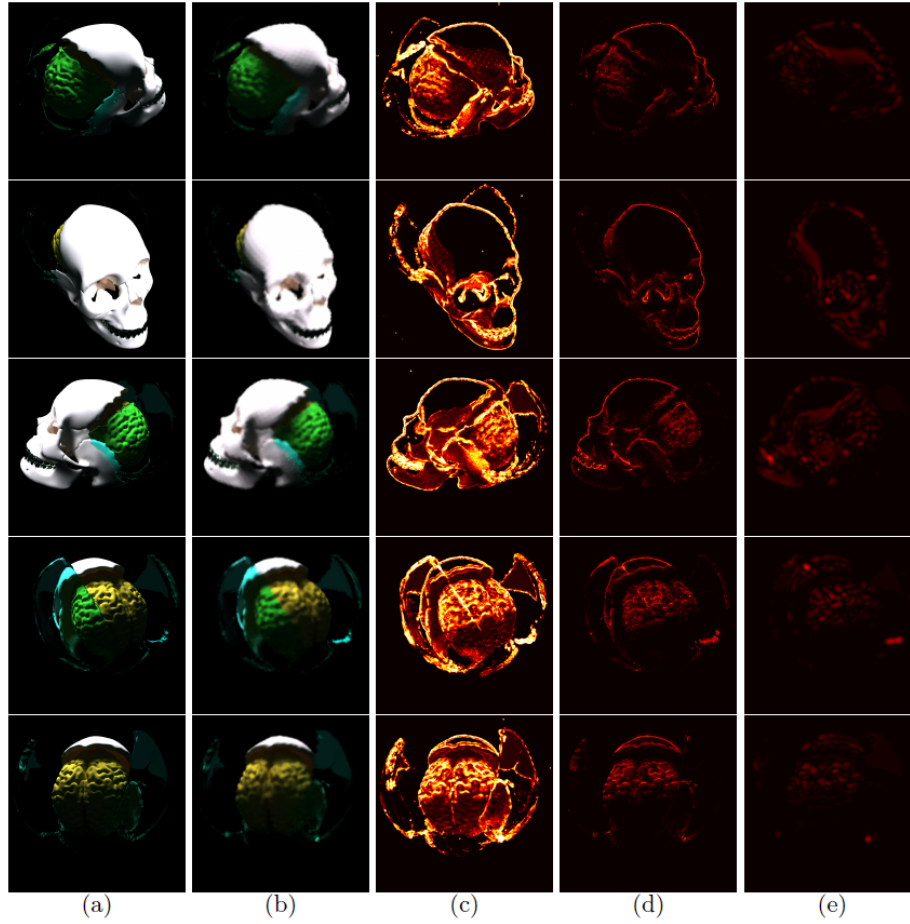


Fig. 4. Rendering results for five different views of our test object (Altered version of [5]) with a distance of 2 units. (a) Conventionally path traced. (b) Images synthesized from our data structure with $M = 12288$, $N = 24576$. (c) SSIM map. Absolute intensity difference of reconstructed images taking into account only (d) higher (0 - 4) (e) and lower levels (0 - 7) of the wavelet decomposition. In (c), (d) and (e) a brighter color indicates a bigger error.

a distance similar to the one showed in Fig. 4, and 2×16 fps in more realistic scenarios with partial cover.

4 Discussion & Conclusion

We have identified several areas for future improvement.

From an image quality point of view, many opportunities lie in the refinement of the image generation process, and in particular, post-rendering corrections. For instance, a known method to improve image based renderings is a view point or parallax correction which takes the distance of a hitpoint to the rendered surface into account [8]. But such a method becomes non-trivial in use cases such as volume rendering, where the depth of hitpoints is ill-defined. However, analyzing the higher frequency components of a LumiPath-based image clearly reveals a deterministic and predictable pattern of the produced artifacts as shown in Fig. 4, suggesting that non-linear filtering, e. g. in the form of a deep neural network, could substantially improve the image quality. Encouraging progress in this regard has been made in the field of learning-based movie restoration and game remastering. Given our described challenges, we believe that a neural network appears to be an appropriate tool to reduce artifacts and enhance overall image quality. More specifically, a shallow fully convolutional neural network with skip ahead connections (U-Net-like [18]) seems applicable, since our learning problem can be fully supervised. Thinking farther ahead, it may even be possible to design a network architecture that directly samples from our plenoptic function to synthesize the desired image and can be trained end-to-end. Such approach would be appealing since o and d can be taken into account during the inference process (which is in contrast to the post-rendering correction envisioned above that operates on already straight-forwardly interpolated radiance values).

While post-rendering corrections are our highest priority as of know, other approaches to improve the image quality can be envisioned as well. A promising complementary approach would be the investigation of non-uniform sampling patterns of the Fibonacci Spheres, e. g. based on object properties such as curvature. However, adaptive sampling of Fibonacci Spheres is complex and requires sophisticated handling of boundaries.

Our current investigations focus on pushing the *LumiPath* image quality via post-rendering correction to keep lightfield sizes below 600 MB, which seems appropriate for today’s embedded devices. We understand our results as promising, exciting, yet preliminary evidence that our LumiPath algorithm can achieve reasonable real-time physically-based rendering results on compute-limited devices such as optical see-through head-mounted displays.

References

1. Siemens Healthineers provides the photorealistic 3D visualization app Cinematic Rendering for Microsoft HoloLens 2. <https://www.healthcare.siemens.com/press-room/press-releases/pr-20190226008shs.html>, accessed: 2019-03-06
2. Adelson, E.H., Bergen, J.R., et al.: The plenoptic function and the elements of early vision (1991)
3. Camahort, E., Leros, A., Fussell, D.: Uniformly sampled light fields. In: Drettakis, G., Max, N. (eds.) *Rendering Techniques '98*. pp. 117–130. Springer Vienna, Vienna (1998)
4. Comaniciu, D., Engel, K., Georgescu, B., Mansi, T.: Shaping the future through innovations: From medical imaging to precision medicine. *Medical Image Analysis* **33**, 19–26 (2016), 20th anniversary of the *Medical Image Analysis journal (MedIA)*
5. Coretti, M.: Study and implementation of a decomposable virtual skull in 54 anatomically correct elements. Thesis, <https://www.blendswap.com/blends/view/90783>
6. Gershun, A.: The light field. *Journal of Mathematics and Physics* **18**(1-4), 51–151 (1939)
7. Geyer, L.L., Schoepf, U.J., Meinel, F.G., Nance Jr, J.W., Bastarrika, G., Leipsic, J.A., Paul, N.S., Rengo, M., Laghi, A., De Cecco, C.N.: State of the art: iterative ct reconstruction techniques. *Radiology* **276**(2), 339–357 (2015)
8. Gortler, S.J., Grzeszczuk, R., Szeliski, R., Cohen, M.F.: The lumigraph. In: *Proceedings of the 23rd Annual Conference on Computer Graphics and Interactive Techniques*. pp. 43–54. SIGGRAPH '96, ACM, New York, NY, USA (1996)
9. Hajek, J., Unberath, M., Fotouhi, J., Bier, B., Lee, S.C., Osgood, G., Maier, A., Armand, M., Navab, N.: Closing the calibration loop: an inside-out-tracking paradigm for augmented reality in orthopedic surgery. In: *International Conference on Medical Image Computing and Computer-Assisted Intervention*. pp. 299–306. Springer (2018)
10. Kajiya, J.T.: The rendering equation. In: *ACM Siggraph Computer Graphics*. vol. 20, pp. 143–150. ACM (1986)
11. Keinert, B., Innmann, M., Sanger, M., Stamminger, M.: Spherical fibonacci mapping. *ACM Trans. Graph.* **34**(6), 193:1–193:7 (Oct 2015)
12. Marques, R., Bouville, C., Ribardiere, M., Santos, L.P., Bouatouch, K.: Spherical fibonacci point sets for illumination integrals. In: *Computer Graphics Forum*. vol. 32, pp. 134–143. Wiley Online Library (2013)
13. McMillan, L., Bishop, G.: Plenoptic modeling: An image-based rendering system. In: *Proceedings of the 22nd annual conference on Computer graphics and interactive techniques*. pp. 39–46. Citeseer (1995)
14. Michael Faraday Esq. D.C.L. F.R.S.: LIV. Thoughts on ray-vibrations. *The London, Edinburgh, and Dublin Philosophical Magazine and Journal of Science* **28**(188), 345–350 (1846)
15. NVidia: Nvidia optix ray tracing engine. NVidia Developer Documentation, <https://developer.nvidia.com/optix>
16. Pharr, M., Jakob, W., Humphreys, G.: *Physically based rendering: From theory to implementation*. Morgan Kaufmann (2016)
17. Rademacher, P.: Ray tracing: Graphics for the masses. *XRDS* **3**(4), 3–7 (May 1997)
18. Ronneberger, O., Fischer, P., Brox, T.: U-net: Convolutional networks for biomedical image segmentation. In: *International Conference on Medical image computing and computer-assisted intervention*. pp. 234–241. Springer (2015)

19. Sampat, M.P., Wang, Z., Gupta, S., Bovik, A.C., Markey, M.K.: Complex wavelet structural similarity: A new image similarity index. *IEEE transactions on image processing* **18**(11), 2385–2401 (2009)
20. Wang, Z., Bovik, A.C.: Modern image quality assessment. *Synthesis Lectures on Image, Video, and Multimedia Processing* **2**(1), 1–156 (2006)
21. Wang, Z., Bovik, A.C., Sheikh, H.R., Simoncelli, E.P., et al.: Image quality assessment: from error visibility to structural similarity. *IEEE transactions on image processing* **13**(4), 600–612 (2004)
22. Zhou, S.K., Engel, K.: Method and system for volume rendering based on 3d image filtering and real-time cinematic rendering (May 29 2018), uS Patent 9,984,493